Piezoelectric Transduction of a Wavelength-Scale Mechanical Waveguide

Yanni D. Dahmani, Christopher J. Sarabalis, Wentao Jiang, Felix M. Mayor, and Amir H. Safavi-Naeini

Phys. Rev. Applied **13**, 024069 — Published 25 February 2020

DOI: 10.1103/PhysRevApplied.13.024069

Piezoelectric transduction of a wavelength-scale mechanical waveguide

Yanni D. Dahmani,* Christopher J. Sarabalis,* Wentao Jiang, Felix M. Mayor, and Amir H. Safavi-Naeini†
Department of Applied Physics and Ginzton Laboratory, Stanford University
348 Via Pueblo Mall, Stanford, California 94305, USA
(Dated: January 22, 2020)

We present a piezoelectric transducer in thin-film lithium niobate that converts a 1.7 GHz microwave signal to a mechanical wave in a single mode of a 1 micron-wide waveguide. We measure a -12 dB conversion efficiency that is limited by material loss. The design method we employ is widely applicable to the transduction of wavelength-scale structures in emerging phononic circuits like those needed for efficient piezo-optomechanical converters and spin-phonon transducers.

I. INTRODUCTION

Phonons interact strongly and coherently with many kinds of degrees of freedom and so can glue together hybrid classical and quantum systems. With efficient electromechanical transducers, we can leverage microwave electronics to readout and control quantum dots [1, 2], color-centers [3, 4], magnons [5], and optical photons [6–16]. Furthermore the phonons themselves are useful for manipulating classical and quantum information. Ultra-high-Q nanomechanical resonators [17] have precipitated a number of new approaches to hardware-efficient quantum information processing [18, 19]. Since mechanical waves are highly confined and slow compared to light, they are apt for low-loss, compact microwave components for storing [20–22], routing [23], delaying [24–26], and filtering [27–29] classical and quantum information.

Many of these applications rely on or benefit from going to smaller mechanical waveguides and resonators. Per phonon, the strain and displacement in a cavity and waveguide scales as the inverse root of the volume and area, respectively. As a result, size plays a central role in improving phonon coupling rates as in optomechanics [30–34] and strain-coupled two-level systems [35]. Moreover, wavelength-scale structures have fewer modes giving more control over loss and coupling. The smaller the waveguide or resonator the better, placing new demands on the design of efficient and mode-selective electromechanical transducers [36–38]. While piezoelectric driving of wavelength-scale structures—both nanobeam resonators [11, 13–15, 39] and waveguides [7, 40]—has been demonstrated, many devices such as nanophotonic acousto-optic modulators [7] and microwave-to-optical quantum converters [14, 15] are still primarily limited by the efficiency of their transducer. An important challenge remains in systematically designing and characterizing wavelength-scale, single-mode transducers as stand-alone phononic components that can be broadly incorporated into phononic networks.

Here we present a piezoelectric transducer at 1.7 GHz that excites the fundamental horizontal shear (SH0) mode of a 1 μm-wide waveguide in thin-film lithium niobate (LN). We recently used these transducers to drive the breathing mode of a nanobeam increasing our previously demonstrated electromechanical efficiency by five orders of magnitude [41].

Our work focuses on a single transducer design in the platform but many of the methods we employ are general. In Section II, we show how the area of a transducer can be estimated from the piezoelectric coupling coefficient k^2_{eff} and the target bandwidth. With large k^2_{eff}, a small transducer can be matched to 50 Ω making it easier to couple to a wavelength-scale waveguide. In Section III, we show that, for shear waves, adiabatic elastic horns cannot be used to generate wide beams. This motivates our narrow designs. In Section IV, we formulate the design problem in terms of the electromechanical scattering matrix and show how the elements of the matrix (in particular, the transmission $t_{\text{b}\mu}$) can be computed by FEM with a normal model decomposition. This S-matrix approach makes it possible to incorporate the transducer into a more general network of microwave electromagnetic and phononic components. In our analysis, we find the best matched transducer is not the most efficient; microwave reflections $|S_{11}|$ cannot be used as a proxy for $|t_{\text{b}\mu}|$. For this reason, our measurements in Section V focus on de-embedding the transducer from a cascaded transducer-waveguide-transducer network giving us a conversion efficiency $|t_{\text{b}\mu}|^2 = 7.0\%$.

II. PIEZOELECTRIC COUPLING CONSTRAINTS ON TRANSDUCER AREA

We begin by considering the area A on the surface of a chip needed to impedance match to a 50 Ω transmission line. The smaller we can make our transducer, the easier it will be to couple to a wavelength-scale waveguide; but the area of the transducer is constrained by the impedance of the transmission line, the desired bandwidth, and the piezoelectric coupling coefficient k^2_{eff}. We show in Appendix A that for a few different models of piezoelectric transducers, these important parameters are

* These authors contributed equally to this work.
† safavi@stanford.edu

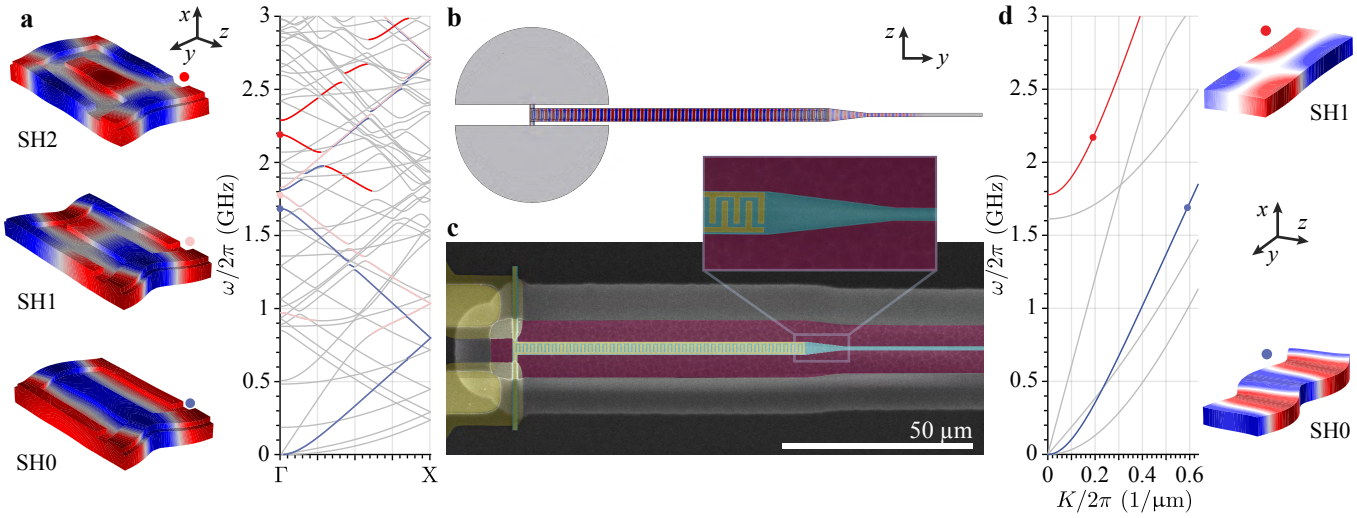

FIG. 1. Suspended transducers patterned in 300 nm-thick, X-cut LN on silicon are designed to excite the SH0 mode of a 1 μm-wide waveguide at 1.7 GHz. They are comprised of a 3.4 μm wide, 100 nm thick aluminum IDT, and a 10 μm-long linear horn. In the false color SEM **c**, LN is blue, aluminum is yellow, and the XeF_2 release etch front is burgundy. FEM analysis **b** shows the horn scatters the SH0 mode of the IDT efficiently into the SH0 mode of the 1 μm-wide waveguide. Bands and Bloch functions of the IDT and waveguide which constitute the asymptotic state of the horn are plotted at left **a** and right **d**, respectively. Waves propagate along y and color indicates displacement along z.

related by the expression

$$A = \frac{\pi}{4}\frac{1}{\omega_s^2 c_s k_{\text{eff}}^2}\int \mathrm{d}\omega\, G(\omega) \tag{1}$$

$$= \frac{\pi^2}{8}\frac{G_0}{\omega_s^2 c_s}\frac{\gamma}{k_{\text{eff}}^2} \quad \text{(for Lorentzian } G(\omega)\text{)}. \tag{2}$$

Here G is the conductance (the real part of the admittance Y) of the interdigital transducer (IDT) ; c_s is the capacitance per unit area; ω_s is the series resonance frequency; G_0 and γ are the maximum and full-width-half-maximum of $G(\omega)$; and the integral is evaluated over an interval about ω_0.

Equation 1 gives us a quick way to estimate device parameters. We see that matching to 50 Ω over a large bandwidth comes at the cost of area. Materials like LN with high $\varepsilon k_{\text{eff}}^2$, where ε is the dielectric permittivity, enable small transducers with large bandwidth. If we only need a small bandwidth, we can make a small, resonant transducer that is easier to couple to a wavelength-scale waveguide. In principle there is no lower bound on the area of a 50 Ω-matched transducer; in practice material and clamping loss sets a minimum γ.

The horizontal shear (SH) waves of an LN slab are strongly piezoelectric enabling small transducers. SH waves traveling along the Y crystal axis in X-cut LN couple to an IDT's electrodes mainly via the $d_{YZY} = 68$ pC/N component of the piezoelectric tensor [42, 43] leading to large k_{eff}^2 up to 35%. The coupling coefficient can be computed for an arbitrary mode of a unit cell of an arbitrary IDT as shown in Appendix B; values for various modes of an LN slab without electrodes are reported by Kuznetsova *et al.* [44].

A 1.9 μm pitch IDT with $c_s = 155$ μF/m^2 and $\omega_s = 2\pi \times 1.7$ GHz (computed by FEM) requires an area of roughly 250 μm^2 to match to 50 Ω over 10 MHz. This bandwidth is consistent with our previous measurements of loss which places a lower bound on bandwidth in the platform [45]. With this area constraint in hand and the intuition that comes with it, we turn our attention to the modes of LN waveguides and the physics of elastic horns.

III. MODES OF AN LN WAVEGUIDE AND ELASTIC HORN DESIGN

A piezoelectric waveguide with continuous translational symmetry such as the rectangular waveguide in Figure 1d supports a power-orthogonal basis of modes at each frequency ω. These modes solve an eigenvalue problem on a 2D cross-section of the waveguide in which the stress $\boldsymbol{\sigma}$ and velocity $\mathbf{v}$ fields of the theory of elasticity and the electrostatic potential Φ of electrostatics are coupled by the piezoelectric tensor $\mathbf{d}$. The modes $|\psi_m\rangle \equiv (\boldsymbol{\sigma}_m, \mathbf{v}_m, \Phi_m)$, indexed by m, vary along the waveguide as $e^{iK_m y}$ for complex eigenvalue K_m. If $K_i \neq K_j^*$, modes i and j are power-orthogonal and satisfy

$$\langle\psi_i|\,\psi_j\rangle \equiv \int \mathrm{d}\mathbf{S}\cdot(-\boldsymbol{\sigma}_i^*\mathbf{v}_j - \boldsymbol{\sigma}_j\mathbf{v}_i^* + i\omega\mathbf{D}_i^*\Phi_j - i\omega\mathbf{D}_j\Phi_i^*) = 0 \tag{3}$$

forming an inner product space in which band structures can be computed and scattering can be studied [46]. Here $\mathbf{D} = -\boldsymbol{\varepsilon}\nabla\Phi + \mathbf{d}\boldsymbol{\sigma}$ is the electric displacement field, and we normalize our basis such that $\langle\psi_i|\,\psi_j\rangle = \delta_{ij}$. For

more detail on our choice of Fourier conventions and the relationship between the inner product and power see Appendix C.

The wavelength-scale LN waveguide we are trying to excite is 1 μm wide and 300 nm thick. It supports four modes between 0 and 1.6 GHz: the Lamb (A0), the horizontal shear (SH0), the first excited Lamb (A1), and the longitudinal (S0) mode [47]. The band structure is plotted in Figure 1d.

From Section II, we know we need a 250 μm^2 IDT and a way to couple it efficiently to the waveguide. A wider IDT provides room for the wires and reduces the impact of material loss (see Section IV). A natural choice then is to expand the mode of the narrow waveguide using a horn structure to couple to a wider IDT. In microwave and acoustic design, adiabatic horns are commonly used to expand a beam, but elastic media have an added phenomenon that spoils this approach: they support surface waves.

If we increase the width of the waveguide adiabatically, the SH0 mode splits and localizes to the edges. This is analogous to how Rayleigh waves localize to a surface. In Figure 2a, we vary the width of the waveguide and compute the wavevectors of the SH modes. The SH0 and SH1 modes of the 1 μm-wide waveguide (left) continuously transition to the degenerate antisymmetric and symmetric edge modes (right), respectively. For shear waves, adiabatic horns cannot produce wide, uniform beams and therefore cannot efficiently convert these waves from a wide IDT to a narrow waveguide.

We choose 3.4 μm for the width of the IDT so that an adiabatically tapered horn can efficiently scatter the transduced mode into the 1 μm waveguide. The narrow IDT allows us to simplify the design, make full use of the width of the transducer, spectrally resolve the SH0 and SH1 modes, and keep spurious shear modes in cutoff.

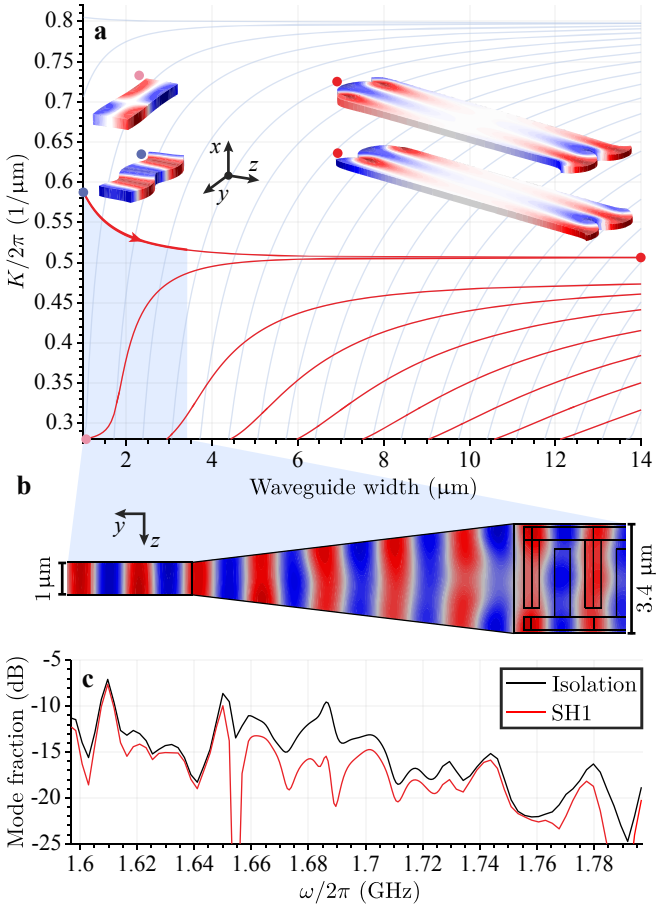

FIG. 2. **a.** Adiabatic elastic horns do not generate wide mechanical beams. The SH0 and SH1 modes (u_z plotted at left) limit to degenerate antisymmetric and symmetric edge supermodes (right), respectively. Below 5 μm the SH waves (red) are well-resolved. The Lamb waves are plotted in light blue. **b.** The linear horn scatters the SH0 mode of the 3.4 μm-wide IDT efficiently into SH0 of the 1 μm-wide output waveguide. **c.** Decomposing the power in the waveguide we find that transduction of spurious modes, the isolation, is better than −10 dB away from the nodes in the conductance over a 200 MHz bandwidth. The largest spurious component is the SH1 mode plotted in red.

IV. FEM MODELS OF THE TRANSDUCER: LOSS LIMITS TRANSMISSION $t_{\mathrm{b}\mu}$

A transducer is often sufficiently characterized by its admittance $Y(\omega)$ and the design objective can be to minimize microwave reflections, *i.e.,* to match to the device. This is true, for example, when loss channels like scattering into bulk can be ignored and the mode structure of the radiation is well understood. But the admittance does not fully characterize the linear response; minimizing microwave reflections does not necessarily maximize the electro-mechanical transmission. Our numerical analysis in this section and measurements in Section V are tailored to maximize and characterize transmission into the SH0 mode, $t_{\mathrm{b}\mu}$.

A 3D FEM analysis of the transducer, IDT and horn as shown in Figure 1b, is used to solve the inhomogenous piezoelectric equations at each frequency. The domain is bordered by a perfectly matched layer. As discussed in Section III, the modes of the output waveguide form an inner-product space (see Appendix D) in which we decompose the power radiated by the IDT and check that the transducer excites a single mode. Given a solution $|\psi\rangle$, the coefficients a_m are computed using Equation 3

$$a_m = \langle \psi_m | \, \psi \rangle \tag{4}$$

such that

$$|\psi\rangle = \sum_m a_m \, |\psi_m\rangle \tag{5}$$

where $|a_m|^2$ is the power in mode m. For each mode m there's an associated backwards propagating mode $-m$, the pair of which form a piezoelectric port. In order to compute $t_{\mathrm{b}\mu}$, we set the voltage across the IDT at each

frequency ω; compute $Y(\omega)$ and a_m; and relate them to a column of the S-matrix, one component of which is $t_{b\mu}$. Details on piezoelectric ports and expressions for the S-matrix can be found in Appendix E.

Our transducer is a 1.92 µm-pitch, 100 nm thick aluminum IDT with a duty cycle of 50%. The IDT's fingers end 300 nm away from the 400 nm wide bus wires that run along the edges of the waveguide. Based on previous measurements in the platform [45], we incorporate a uniform material loss tangent corresponding to $Q_i = 300$ and scale the piezoelectric tensor from its bulk values by 0.67. The SH0 and SH2 Γ-point modes of the IDT (Figure 1a) are efficiently transduced and scattered into the SH0 and SH1 modes of the waveguide (Figure 1d). In what follows, we focus on the SH0 mode of the IDT but have recently used the SH2 response to drive the breathing mode of a nanobeam [41].

Our analysis in Section III suggests the 10 µm long linear horn shown in Figure 2b will function approximately adiabatically. Over a large bandwidth, over 90% of the power transmitted into the waveguide is transmitted into the SH0 mode. Less than −10 dB goes into spurious modes (labeled *isolation* in Figure 2c). Excluding nodes in the conductance, power in the largest spurious mode (SH1) remains below −15 dB over 200 MHz.

In Figure 3, we analyze how impedance matching and damping contribute to $t_{b\mu}$ for transducers of different lengths. At first as N increases, the microwave reflections drop and the transmission improves as expected. But improvements in matching to the transmission line compete with damping in the IDT. This is seen in the fraction of the dissipated energy which is lost due to intrinsic damping (Figure 3b). Above an optimal N, the transmission $t_{b\mu}$ decreases even as microwave reflections continue to drop. These competing effects lead to a maximum in $|t_{b\mu}|^2$ for an optimal N (Figure 3c): 12% for 29 finger pairs with $Q_i = 300$. In short, minimizing S_{11} does not always maximize $t_{b\mu}$. Also, $t_{b\mu}$ is larger in transducers with lower dissipation (larger Q_i).

For $Q_i = 300$, intrinsic damping in the transducer is the dominant loss channel with only a small fraction of the energy lost to the tethers. Of the total power dissipated $2G(\omega)|V(\omega)|^2$ by an $N = 40$ transducer like those measured in Section V, 11% is emitted into the waveguide, 96% of which is in the SH0 mode. Only 5% is lost to clamping from the tethers along the back edge while the other 84% is lost to intrinsic damping.

There are a few approaches to improve $|t_{b\mu}|^2$ beyond 12%. The most obvious is to improve the material parameters k^2_{eff} and Q_i (Figure 3c). For applications in quantum science, operating at cryogenic temperatures will likely increase Q_i by suppressing thermally induced mechanical loss and ohmic dissipation in the electrodes. Another strategy is to reduce the reflection coefficient at the IDT-waveguide interface reducing the influence of resonance and allowing us to make longer transducers before reaching loss-limits. Lastly we could diverge from the low width, low density of states design and employ wider waveguides, embracing the challenges of multi-mode design [39, 40].

V. MEASUREMENTS

Starting with a 500 nm-thick film of LN on a 500 µm-thick silicon substrate, the film is thinned to 300 nm by argon milling before patterning an HSQ mask with e-beam lithography to define the waveguides. The mask is transferred to the LN by angled argon milling [15]. We then perform an acid clean to remove resputtered, amorphous LN. We deposit 100 nm of Al for electrodes and 200 nm Al for contact pads by e-beam lithography and photolithography, respectively; metal evaporation; and liftoff. Finally we release the structures with a masked XeF_2 dry etch.

The S-parameters of the transducers are measured with a vector network analyzer (Rhode & Schwarz ZNB20) on a probe station calibrated to move the reference plane to the tips of the probes (GGB nickel 40A). Several modes below 10 GHz are strongly transduced as seen in the S_{11} plotted in Figure 4. The conductance

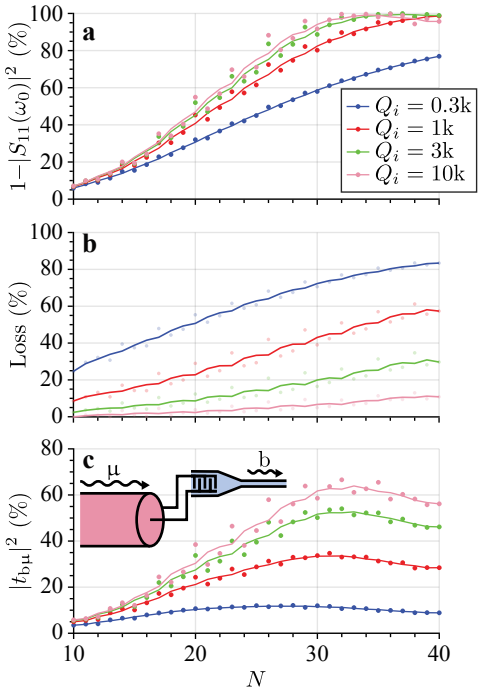

FIG. 3. By computing the linear response $Y(\omega)$ and decomposition $\{a_m\}$ we study the N-dependence of the transmission $t_{b\mu}$ from a 50 Ω transmission line to the SH0 mode. **a.** Microwave reflections S_{11} decrease with N. Lower loss devices are matched with smaller N. **b.** As reflections drop, the fraction of the total power lost increases, diminishing transmission into the SH0 mode. **c.** These competing effects lead to an optimal N for maximizing $|t_{b\mu}|^2$ which increases with Q_i. Numerical results (points) are smoothed with a moving window average (curve) for clarity.

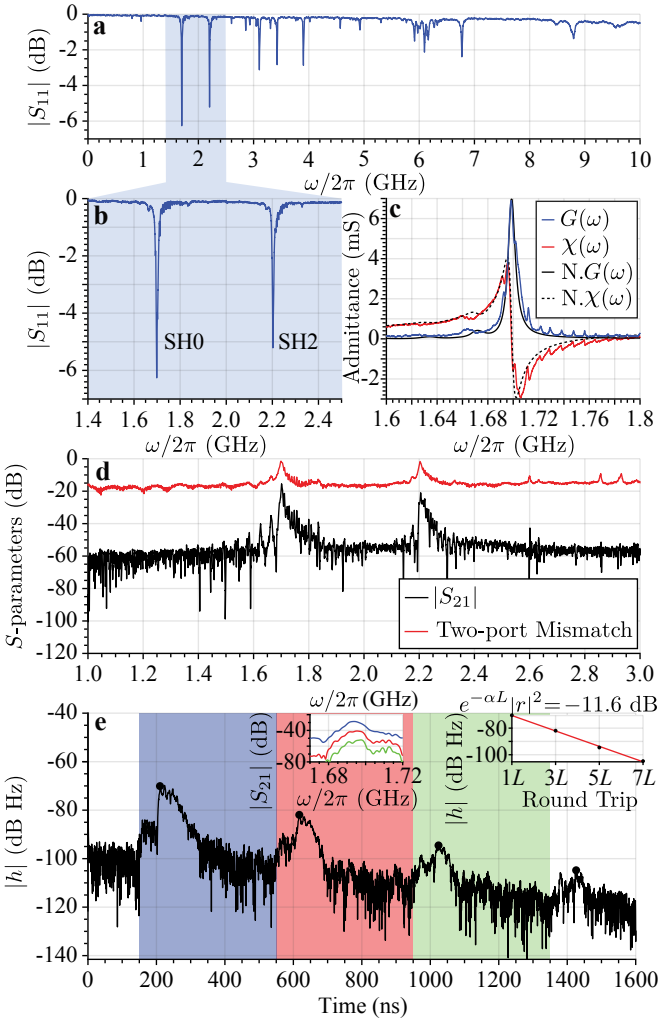

FIG. 4. **a.** The $|S_{11}|$ of an $N = 40$ transducer restricted to the SH0 and SH2 responses in **b**. **c.** The conductance G and susceptance χ of the SH0 mode are overlaid on FEM results. **d.** The $|S_{21}|$ of an ideal delay line with no insertion loss would equal the two-port mismatch $1-|S_{11}|^2/2-|S_{22}|^2/2$ in red (see Appendix G). **e.** For $L = 800$ µm, the heights of the echoes in the impulse response are fit (inset) to extract the round trip loss. We filter the echoes (intervals shaded blue, red, and green) to compute the single, triple, and quintuple-transit S_{21} plotted with corresponding colors (inset) used to extract $|t_{b\mu}|$ as described in Section V.

$G \equiv \mathrm{Re}Y$ and susceptance $\chi \equiv -\mathrm{Im}Y$ for the SH0 mode plotted in Figure 4c match well with the overlaid simulated curve and Γ-point frequency of the IDT unit cell bands shown in Figure 1a. The peak conductance and full-width-half-max for the SH0 mode, 6.5 mS and 9.7 MHz inferred by Lorentzian fit, agree with our models, 6.9 mS and 7.3 MHz. We infer a static capacitance of 31 fF by fit to the DC response of χ and use it along with the conductance fit by Equation 2 to calculate a k^2_{eff} of 15% (17% computed in Appendix B). From the exact expression in Appendix A, we find $k^2_{\mathrm{eff}} = 12\%$ (14.6% simulated). This is decreased by the feedthrough capacitance of the contact pads.

In order to characterize the transducer, we need to extract $t_{b\mu}$ from measurements of S_{21}. To this end, we de-embed the transducer from the transducer-waveguide-transducer two-port network by analyzing its response in the time-domain. Consider a device with an $L = 200$ µm long waveguide. If we were to infer $t_{b\mu}$ directly from the $|S_{21}|$ shown in Figure 4d by halving the −15.7 dB peak, we would come to the unlikely conclusion that our transducer in practice is more efficient than in simulation. This is because at 1.7 GHz, reflections at the IDT-waveguide interface resonantly enhance transmission through the waveguide. The transmission coefficient $t_{b\mu}$ cannot be deduced directly from the $|S_{21}|$ of a short device with large reflections at the IDT interface.

Instead, we isolate the propagation loss α and $t_{b\mu}$ by analyzing the time-domain impulse response $h(t)$, the inverse Fourier transform of $S_{21}(\omega)$, plotted for a device with $L = 800$ µm (Figure 4e). The first pulse takes the shortest path through the device and is attenuated by $|t_{b\mu}|^2 e^{-\alpha L/2}$. Each subsequent echo takes an additional round trip, is attenuated by $|r|^2 e^{-\alpha L}$, and delayed by $2L/v_g = 4.0 \times 10^2$ ns. We fit $|r|^2 e^{-\alpha L} = -11.6$ dB from the peaks in Figure 4e and transform the first pulse (blue) back to the frequency domain (inset) to find $|t_{b\mu}|^2 e^{-\alpha L/2} = -28.6$ dB. More detail is provided in Appendix F.

The single-transit and round-trip loss are two constraints on three unknown quantities: $|t_{b\mu}|^2$, $|r|^2$, and α. By sweeping the length of the device, all three parameters can be determined independently. In lieu of a length sweep, we ignore scattering into other modes and assume $|t_{b\mu}|^2 + |r|^2 = 1$ at the IDT-waveguide interface to find a $|t_{b\mu}|^2$ of 7.0% (comparable to the simulated value of 8.9% for $N = 40$), an $|r|^2$ of 93%, and an α of 6.8 dB/mm.

Given the measured group velocity of $v_g = 4.0 \times 10^3$ m/s, this α corresponds to a quality factor $Q = \omega_0/\alpha v_g$ of 1700 in the waveguide and an $f_0 Q$ of 2.9×10^{12} which is comparable to our previous work in multi-moded, high frequency delay lines with an $f_0 Q$ of 4.6×10^{12} [45]. We see an order of magnitude improvement over delay lines in suspended LN employing the S0 mode at 350 MHz where $f_0 Q = 0.45 \times 10^{12}$ [48]. Resonators using antisymmetric thickness modes exhibit $f_0 Q$ products over twice as large (9.15×10^{12}) [49].

VI. CONCLUSIONS

In suspended LN films, large reflections at the IDT-waveguide interface lead to resonance. These reflections distort signals in a filter or delay line and reduce bandwidth; here, resonance allows us to make small transducers and use simple horns to couple to a waveguide. This reduced bandwidth can be tolerated in microwave-to-optical conversion and two-level system control and readout if it facilitates high conversion efficiency. At

cryogenic temperatures, intrinsic loss will likely drop, increasing the conversion efficiency of our design and enabling smaller bandwidths and therefore smaller transducers. At room temperature, the route to more efficient designs calls for wider transducers and efficient horns.

The design of a horn depends on the details of a given platform. For example, coupling surface acoustic waves to suspended waveguides and beams [39] introduces new features to the design like mitigating reflections at the slab interface. The S-matrix formulation described here can be applied generally to design and characterize phononic components, such as horns, in a variety of platforms.

Our hope is that insights from our design of a phononic waveguide transducer in suspended LN can be generally applied to selectively exciting modes of wavelength-scale mechanical devices and that the methods we employed can inform approaches to design and characterization of phononic components and systems.

ACKNOWLEDGEMENTS

The authors would like to thank Rishi N. Patel, Patricio Arrangoiz-Arriola, and Timothy P. McKenna for useful discussions. This work was supported by a MURI grant from the U. S. Air Force Office of Scientific Research (Grant No. FA9550-17-1-0002), by a fellowship from the David and Lucille Packard foundation, and by the National Science Foundation through ECCS-1808100 and PHY-1820938. Part of this work was performed at the Stanford Nano Shared Facilities (SNSF), supported by the National Science Foundation under Grant No. ECCS-1542152, and the Stanford Nanofabrication Facility (SNF).

Appendix A: Relating the piezoelectric coupling coefficient to the net conductance

In Section II, we relate the area of a transducer to the piezoelectric coupling coefficient k^2_{eff}, the static capacitance per unit area c_s, and the net conductance

$$A = \frac{\pi}{4}\frac{1}{\omega_0^2 c_\text{s} k^2_{\text{eff}}}\int \text{d}\omega\, G\left(\omega\right) \tag{A1}$$

with conductance $G \equiv \text{Re}Y(\omega)$. In this Appendix, we show how this expression holds for two very different models of piezoelectric transducers: the Butterworth-Van Dyke circuit model and the impulse response model of a SAW transducer [50]. We consequently take this expression as our device-independent and easily computable *definition* of k^2_{eff}.

1. Review of Butterworth-Van Dyke

The Butterworth-Van Dyke (BVD) circuit model is a simple, widely used model of a piezoelectric resonator. The circuit is comprised of a static capacitance C_0 in parallel with a motional series LC with motional inductance L_m and capacitance C_m. It is equivalent to the circuit in Figure 5 for $R_\text{m} = 0$.

The BVD circuit with admittance [51]

$$Y\left(\omega\right) = -i\omega C_0 - i\omega C_\text{m}\frac{1}{1-\omega^2/\omega_\text{s}^2} \tag{A2}$$

exhibits a pole at the series resonance frequency $\omega_\text{s} \equiv 1/\sqrt{L_\text{m}C_\text{m}}$. Similarly, the impedance diverges at the parallel resonance frequency ω_p where $Y(\omega_\text{p}) = 0$. Setting Equation A2 to zero and solving for ω_p we find

$$\omega_\text{p} = \omega_\text{s}\sqrt{1+\frac{C_\text{m}}{C_0}}. \tag{A3}$$

The splitting between the series and parallel resonance frequencies increases with the ratio of motional and static capacitance.

For a resonator, the effective piezoelectric coupling coefficient is defined in terms of the ratio of ω_s and ω_p [52, 53]

$$k^2_{\text{eff}} = \frac{\pi}{2}\frac{\omega_\text{s}}{\omega_\text{p}}\left[\tan\left(\frac{\pi}{2}\frac{\omega_\text{s}}{\omega_\text{p}}\right)\right]^{-1}. \tag{A4}$$

To second order in $\left(\omega_\text{p}-\omega_\text{s}\right)/\omega_\text{p}$ the coupling coefficient is

$$k^2_{\text{eff}} = \frac{\pi^2}{4}\frac{\omega_\text{s}}{\omega_\text{p}}\left(1-\frac{\omega_\text{s}}{\omega_\text{p}}\right) \tag{A5}$$

as in [54] and to first order

$$k^2_{\text{eff}} = \frac{\pi^2}{4}\left(1-\frac{\omega_\text{s}}{\omega_\text{p}}\right). \tag{A6}$$

In the next section, we show that the motional capacitance C_m is proportional to the net conductance. Ultimately we want to relate the net conductance, which is a convenient form for expressing design specifications, to the area of the transducer using intensive quantities like ω_s, ω_p, and k^2_{eff}. To do this, it is helpful to note the capacitance ratio from Equation A3

$$\frac{C_\text{m}}{C_0} = \frac{\omega_\text{p}^2}{\omega_\text{s}^2} - 1 \tag{A7}$$

can be re-expressed to first order in $\left(\omega_\text{p}-\omega_\text{s}\right)/\omega_\text{p}$

$$\begin{aligned} k^2_{\text{eff}} &= \frac{\pi^2}{8}\left(\frac{\omega_\text{p}^2}{\omega_\text{s}^2}-1\right) \\ &= \frac{\pi^2}{8}\frac{C_\text{m}}{C_0} \end{aligned} \tag{A8}$$

as in [55].

2. Modified Butterworth-Van Dyke circuit model

In order to relate the net conductance to C_m, we begin with the lossy resonator with motional resistance R_m diagrammed in Figure 5.

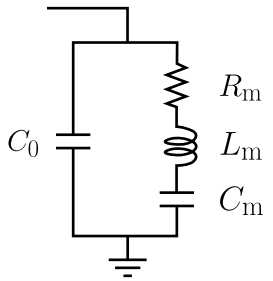

FIG. 5. Butterworth-Van Dyke circuit modified to include mechanical loss.

The admittance of this circuit

$$\begin{aligned} Y(\omega) &= -i\omega C_0 + \frac{1}{\frac{1}{-i\omega C_\mathrm{m}} - i\omega L_\mathrm{m} + R_\mathrm{m}} \\ &= -i\omega C_0 + i\omega_\mathrm{s}^2 C_\mathrm{m} \frac{\omega}{\omega^2 + i\omega_\mathrm{s}\omega/Q - \omega_\mathrm{s}^2} \end{aligned} \tag{A9}$$

is conveniently expressed in terms of the series resonance frequency $\omega_\mathrm{s} \equiv 1/\sqrt{L_\mathrm{m} C_\mathrm{m}}$ and the quality factor $Q^{-1} \equiv \omega_\mathrm{s} R_\mathrm{m} C_\mathrm{m}$. From Equation A9 we directly compute $G(\omega)$ and the net conductance relating it to k_eff^2 to derive Equation A1.

We can simplify the calculation by expanding the motional term as a sum of first order poles

$$Y(\omega) = -i\omega C_0 + Y_+(\omega) + Y_-(\omega). \tag{A10}$$

The admittance of the pole at frequency

$$\omega_\pm \equiv \pm\omega_\mathrm{s}\sqrt{1 - 1/4Q^2} - i\omega_\mathrm{s}/2Q \tag{A11}$$

is

$$Y_\pm(\omega) = \pm\frac{i\omega_\mathrm{s}^2 C_\mathrm{m}}{2\omega_0} \frac{\omega}{\omega \mp \omega_0 + i\omega_\mathrm{s}/2Q}. \tag{A12}$$

For compactness, we have introduced a modified series resonance frequency $\omega_0 \equiv \omega_\mathrm{s}\sqrt{1 - 1/4Q^2}$.

Taking the real part of Y, we find the conductance

$$G(\omega) = G_+(\omega) + G_-(\omega) \tag{A13}$$

where

$$G_\pm(\omega) = \pm\frac{\omega_\mathrm{s}^3 C_\mathrm{m}}{4Q\omega_0} \frac{\omega}{(\omega \mp \omega_0)^2 + \omega_\mathrm{s}^2/4Q^2}. \tag{A14}$$

The conductance is positive and even $G(-\omega) = G(\omega)$.

Focusing on the positive pole, we recognize the net conductance as the mean of a Lorentzian by changing variables $\omega = \omega_\mathrm{s} x/2Q$

$$\begin{aligned} \int_{-\infty}^{\infty} \mathrm{d}\omega G_+(\omega) &= \frac{\pi\omega_\mathrm{s}^3 C_\mathrm{m}}{4Q\omega_0} \left[\frac{1}{\pi}\int_{-\infty}^{\infty} \mathrm{d}x \frac{x}{(x - 2Q\omega_0/\omega_\mathrm{s})^2 + 1}\right] \\ &= \frac{\pi\omega_\mathrm{s}^2 C_\mathrm{m}}{2}. \end{aligned} \tag{A15}$$

Despite being an integral of dissipation by the circuit, the net conductance is completely independent of R_m.

Each pole contributes $\pi\omega_\mathrm{s}^2 C_\mathrm{m}/2$ to the net conductance. Since the conductance is even,

$$\int_{-\infty}^{0} \mathrm{d}\omega G(\omega) = \int_{0}^{\infty} \mathrm{d}\omega G(\omega) \tag{A16}$$

$$= \frac{\pi\omega_\mathrm{s}^2 C_\mathrm{m}}{2}. \tag{A17}$$

By Equation A8, the coupling coefficient is

$$k_\mathrm{eff}^2 = \frac{\pi}{4}\frac{1}{\omega_\mathrm{s}^2 C_0}\int_0^\infty \mathrm{d}\omega G(\omega) \tag{A18}$$

to first order in $(\omega_\mathrm{p} - \omega_\mathrm{s})/\omega_\mathrm{p}$. Devices are usually multimoded. To exclude contributions to k_eff^2 from other modes, we integrate $G(\omega)$ in a narrow band about ω_0.

In Equation A18, C_0 is the product of the static capacitance per unit area c_s defined in the text and the area of the transducer A. A simple rearrangement gives Equation 1

$$A = \frac{\pi}{4}\frac{1}{\omega_\mathrm{s}^2 c_\mathrm{s} k_\mathrm{eff}^2}\int \mathrm{d}\omega G(\omega) \tag{A19}$$

where the integral is evaluated in an interval about ω_s.

Equation A18 and Equation A19 use an approximate form for k_eff^2. We can write these expressions exactly using Equation A7,

$$\int \mathrm{d}\omega G(\omega) = \frac{\pi}{2}\left(\omega_\mathrm{p}^2 - \omega_\mathrm{s}^2\right) C_0 \tag{A20}$$

and

$$A = \frac{2}{\pi}\frac{1}{\left(\omega_\mathrm{p}^2 - \omega_\mathrm{s}^2\right) c_\mathrm{s}}\int \mathrm{d}\omega G(\omega). \tag{A21}$$

Without making any approximations, Equation A21 gives the area in terms of the net conductance and intensive quantities that can be easily calculated for a unit cell of a transducer (Appendix B).

Before moving on to the impulse response model, we consider the traditional BVD circuit discussed in Section A 1 which we will encounter in Appendix B. In Equation A2, the conductance—and therefore the net conductance—is zero. This seems like a problem for Equation A18. On the other hand, the net conductance derived above (Equation A15) is independent of R_m and in the limit $R_\mathrm{m} \to 0$, the circuits are equivalent.

Taking the limit of Equation A14, we find

$$\lim_{Q\to\infty} G_{\pm}(\omega) = \frac{\pi\omega_s^2 C_m}{2}\delta(\omega \mp \omega_0). \tag{A22}$$

In this limit, the admittance in Equation A9 becomes

$$\begin{aligned} Y(\omega) = &-i\omega C_0 + i\frac{\omega_s^2 C_m}{2}\left[\frac{1}{\omega-\omega_s}+\frac{1}{\omega+\omega_s}\right] \\ &+ \frac{\pi\omega_s^2 C_m}{2}\left[\delta(\omega-\omega_s)+\delta(\omega+\omega_s)\right]. \end{aligned} \tag{A23}$$

from which Equation A18 follows.

In contrast to Equation A2, the expression above satisfies the Kramers-Kronig relations. For any causal circuit, the susceptance $\chi(\omega) \equiv -\mathrm{Im}Y(\omega)$ is related to $G(\omega)$ by [56]

$$\chi(\omega) = \frac{1}{\pi}P\int_{-\infty}^{\infty} \mathrm{d}\omega' \frac{G(\omega')}{\omega'-\omega}. \tag{A24}$$

which the delta-function-pole pairs in Equation A23 satisfy.

3. Impulse response model of SAW transducer

The impulse response model (IRM) is a simple model of piezoelectric transduction of a manifold of propagating modes—a band—rather than the resonant degrees of freedom described by the BVD circuit. The conductance of a transducer from the IRM is $G(\omega) = G_+(\omega) + G_-(\omega)$ where [50]

$$G_+(\omega) = 8k_{\mathrm{eff}}^2 f_s C_0 N \frac{\sin^2 X}{X^2}, \tag{A25}$$

$X = \pi N(\omega-\omega_s)/\omega_s$, and $\omega_s = 2\pi f_s$. A similar expression follows for the negative frequency response G_- centered at $-\omega_s$. Since

$$\int_{-\infty}^{\infty} \mathrm{d}X \frac{\sin^2 X}{X^2} = \pi, \tag{A26}$$

we can integrate $G(\omega)$ about ω_s changing variables from ω to X to find

$$\int \mathrm{d}\omega G(\omega) = 16\pi f_s^2 C_0 k_{\mathrm{eff}}^2. \tag{A27}$$

Again the static capacitance can be related to quantities in the main text, $C_0 = Ac_s$, from which it follows

$$A = \frac{\pi}{4}\frac{1}{\omega_s^2 c_s k_{\mathrm{eff}}^2}\int \mathrm{d}\omega G(\omega). \tag{A28}$$

This is Equation 1.

4. Using the net conductance to evaluate the piezoelectric coupling coefficient

Equation A18 expresses the piezoelectric coupling coefficient k_{eff}^2 in terms of quantities that can be directly measured—$G(\omega)$, ω_s, and C_0—without any appeals to a model. This expression comes with a couple caveats. The first is that it does not discriminate between dissipation from mechanisms like ohmic loss and dissipation from radiation into mechanical waves. If Equation A18 is used to calculate k_{eff}^2, care has to be taken to exclude non-mechanical loss mechanisms. Second, the interval of integration for the net conductance $\int \mathrm{d}\omega G(\omega)$ has to be chosen carefully. All modes of a resonator or bands of a SAW transducer in the interval will contribute to the piezoelectric coupling in Equation A18. Finally, Equation A18 is correct only to first order in $(\omega_p - \omega_s)/\omega_p$. For large coupling, it is better to use Equation A20 to compute the resonance frequency ratio ω_s/ω_p which can then be plugged into Equation A4.

Appendix B: Evaluating k_{eff}^2 on a unit cell of a waveguide

In Section II, we begin our design process by using the piezoelectric coupling coefficient k_{eff}^2 and the expression described in Appendix A to estimate the area needed to match to 50 Ω. It is well known that SH waves in X-cut lithium niobate exhibit large k_{eff}^2 and there are numbers for suspended films available [44]. For an arbitrary material stack and waveguide geometry, transducer design begins with a study of k_{eff}^2. Here we show how we calculate k_{eff}^2 for a mode of a wavelength-scale transducer. These methods can be used to study the angle-dependence of k_{eff}^2 in anisotropic media, coupling of different modes of a waveguide, or the influence of geometry such as waveguide dimensions, electrode thickness, *etc.*

The unit cell of the transducer is shown in Figure 6a. Floquet boundary conditions are imposed on the faces normal to the direction of propagation $\hat{y}$. Here we study the Γ-point solution and so the wavevector K along $\hat{y}$ is set to 0. The frequencies of the modes supported in the unit cell under this constraint are plotted in the bands in Figure 1. We compute the admittance $Y(\omega)$ for this domain, setting the voltage across the IDT to 1 V and solving the inhomogenous piezoelectric equations by FEM.

Each mode gives rise to a pole in the susceptance which can be fit to extract the residue G_Σ/π and therefore k_{eff}^2. Here G_Σ is the contribution to the net conductance from the pole. Ignoring contributions from other modes, the susceptance takes the form

$$\chi(\omega) = \omega C_0 + \frac{G_\Sigma}{\pi}\frac{1}{\omega_s-\omega}. \tag{B1}$$

We can independently compute the static capacitance C_0 and the series resonance frequency ω_s and put the problem of finding G_Σ into the form of a linear regression.

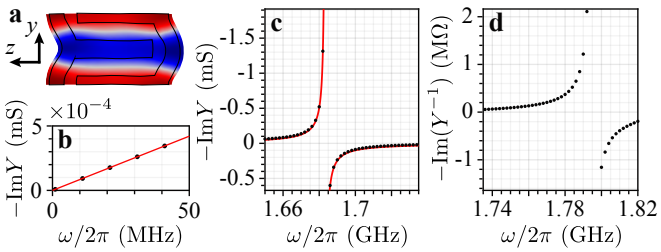

FIG. 6. **a.** The SH mode of a unit cell of the transducer. **b.** The response near DC is fit for the static capacitance C_0. **c.** The pole in the susceptance centered at the series resonance frequency f_s is fit for the net conductance and used with C_0 to compute k^2_{eff}. **d.** In addition to the pole in the admittance, there's a pole in the reactance centered at the parallel resonance frequency f_p.

The series resonance frequency ω_s for each mode can be computed by solving the same eigenvalue problem solved to compute the bands in Figure 1. Here $f_s = 1.683$ GHz. The static capacitance C_0 can be extracted from $\chi(\omega)$ by fitting a line to the low frequency response. The capacitance per unit cell is 1.339 fF. Then we rewrite Equation B1 as a linear regression

$$\frac{G_\Sigma}{\pi} = x \setminus y \tag{B2}$$

with $y = \chi - \omega C_0$ and $x = (\omega_s - \omega)^{-1}$. This regression can be generalized to multiple modes by replacing x with a matrix X with each column $(\omega_{s,i} - \omega)^{-1}$ corresponding to the ith pole with frequency $\omega_{s,i}$.

From the fit in Figure 6c we find $G_\Sigma = 32.91\times10^3$ S Hz per unit cell. We can use G_Σ directly to compute the area needed to match to 50 Ω. By Equation A18, we find a k^2_{eff} of 17.26%. This approximate value for k^2_{eff} holds only to first order in $(\omega_p - \omega_s)/\omega_p$. If we want to use G_Σ to compute k^2_{eff} exactly, we can use the form in Equation A20 to find the resonance frequency ratio ω_p/ω_s which we plug into Equation A4 to find $k^2_{\text{eff}} = 14.70\%$.

There is an easier way to calculate k^2_{eff} for a unit cell directly in terms of ω_s and ω_p. In the absence of material loss, the admittance and reactance diverge at the series and parallel resonance frequencies as seen in Figure 6c and d, respectively. A divergent admittance means the voltage drop across the electrodes is zero. This is consistent with boundary conditions that short the IDT. Imposing these boundary conditions and solving for the eigenmodes of the unit cell at the Γ-point we find $f_s = 1683$ MHz for the SH mode. This is the same frequency as in the bands in Figure 1a. Similarly, the divergent impedance is consistent with an open terminal—floating boundary conditions for the electrodes—and solving for the eigenfrequency of the SH mode we find $f_p = 1795$ MHz.

To first order in $(\omega_p - \omega_s)/\omega_p$ by Equation A8, we find

$$k^2_{\text{eff}} = \frac{\pi^2}{8}\left(\frac{\omega_p^2}{\omega_s^2} - 1\right) \tag{B3}$$

$$= 16.97\%. \tag{B4}$$

which can be used in Equation A1. This agrees well with the fit of the pole. Using ω_s/ω_p to compute k^2_{eff} from the definition (Equation A4), we find $k^2_{\text{eff}} = 14.48\%$.

If material loss is added to the domain, the admittance and impedance no longer diverge and the series and parallel resonances no longer correspond to short and open terminal boundary conditions on the electrodes. In such a case, the net conductance can be computed directly rather than fitting the susceptance as described above.

We note that in a finite transducer, the wave excited by the transducer is only approximated by the Γ-point mode. The wave in a transducer exhibits a spatially-varying envelope [45] in contrast to the Γ-point mode which describes a uniform wave in an infinite transducer. The coupling coefficient k^2_{eff} decreases away from the Γ-point because of mismatch between the wavevector K and the period of the electrodes a, and so this method gives us an upper-bound on k^2_{eff}.

Appendix C: Power Dissipation in the Fourier Domain

The voltage $V(t)$ can be expressed in the frequency domain

$$V(\omega) = \frac{1}{2\pi}\int_{-\infty}^{\infty} \mathrm{d}t\, V(t) e^{i\omega t} \tag{C1}$$

and similarly for current I and admittance Y. With our choice of Fourier convention, the power dissipated by an electrical element $\mathcal{P}(t) = V(t)I(t)$ is the convolution of $V(\omega)$ and $I(\omega)$ in the frequency domain. Averaging this quantity in time extracts the DC component of the spectrum thus reducing the convolution to

$$\langle \mathcal{P} \rangle = \int_{-\infty}^{\infty} \mathrm{d}\omega\, V(\omega) I(-\omega). \tag{C2}$$

Since the voltage is a real-valued quantity, $V^*(\omega)$ is equal to $V(-\omega)$ (the same argument holds for $I(\omega)$ and $Y(\omega)$). Changing our limits of integration and using Ohm's law, $I(\omega) = Y(\omega)V(\omega)$, we find

$$\langle \mathcal{P} \rangle = \int_0^{\infty} \mathrm{d}\omega\, \left(Y^*(\omega) + Y(\omega)\right) |V(\omega)|^2 . \tag{C3}$$

Since $2\mathrm{Re}(Y)(\omega) = 2G(\omega) = Y(\omega) + Y^*(\omega)$, the time average power dissipated by the electrodes is

$$\mathcal{P}_0 = 2\int_0^{\infty} \mathrm{d}\omega\, G(\omega) |V(\omega)|^2 . \tag{C4}$$

To determine the time-average power for a piezoelectric wave, we repeat the previous analysis starting from the instantaneous piezoelectric Poynting vector

$$\mathcal{P}_{\text{piezo}}(t) = -\boldsymbol{\sigma}(t)\mathbf{v}(t) + \Phi(t)\partial_t \mathbf{D}(t) \tag{C5}$$

and find the time-average piezoelectric power

$$\mathcal{P}_{\text{piezo}} = \int_0^\infty d\omega \int d\mathbf{S}\cdot(-\boldsymbol{\sigma}^*\mathbf{v} - \boldsymbol{\sigma}\mathbf{v}^* + i\omega\mathbf{D}^*\Phi - i\omega\mathbf{D}\Phi^*). \tag{C6}$$

We compare this expression to the inner product in Equation 3 to confirm $|a_m|^2$ is the time-average power in mode m. We note that our time-average power differs from that of Auld's by a factor of 1/4 [46] resulting from differences in Fourier conventions. All values reported are power ratios and thus factors of 2 from choices of convention drop out.

Appendix D: Basis

Decomposition of the mechanical energy radiated into a waveguide is necessary for calculating transmission coefficients like $t_{\text{b}\mu}$ needed to characterize a phononic component. For completeness we briefly describe the basis of propagating modes in a 300 nm thick, 1 µm-wide, X-cut LN, rectangular waveguide. We categorize the five 1.7 GHz modes as Lamb (A), horizontal shear (SH), and longitudinal (S) modes which differ in their principal strains S_{xz}, S_{yz}, and S_{zz}, respectively. These modes are plotted in Figure 7 along with their reflection symmetries (σ_z, σ_x) where $(+,-)$, for example, means symmetric and antisymmetric with respect to reflection across the xy and yz-planes, respectively.

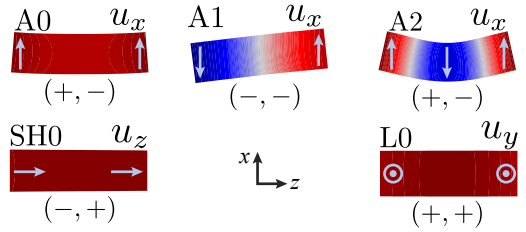

FIG. 7. Modes of an LN waveguide at 1.7 GHz. Color in these plots visualize the dominant displacement field. Light blue arrows show the direction of displacement.

Appendix E: Computing the S-matrix

In our FEM analysis, we are solving a set of inhomogenous equations describing the behavior of our piezoelectric device. The drive term of these equations is a vector $(V, \mathbf{a}_-)^\top$ where V is the voltage across the leads of our transducer and $\mathbf{a}_-$ is a vector of coefficients for the piezoelectric waves incident on the domain as defined by Equation 4.

The solutions of these equations can be represented in matrix form

$$\begin{pmatrix} I \\ \mathbf{a}_+ \end{pmatrix} = \begin{pmatrix} Y & \mathbf{x}_1^\top \\ \mathbf{x}_2 & \text{X} \end{pmatrix} \begin{pmatrix} V \\ \mathbf{a}_- \end{pmatrix}. \tag{E1}$$

The scalar Y is the admittance of the transducer. For M modes, $\mathbf{x}_1$ and $\mathbf{x}_2$ are vectors with M components and X is an $M \times M$ matrix. For the simulations reported here, the coefficients of $\mathbf{a}_-$ are set to 0 and we solve for the first column of the matrix in Equation E1 in terms of the input voltage V.

In order to study how these transducers behave in phononic networks—for example, the two-port transmission devices we use to measure $t_{\text{b}\mu}$—we want to transform the matrix in Equation E1 into a scattering matrix S. To do so, we reexpress V and I in terms of the microwave amplitudes $a_{\pm\mu}$ which we abbreviate to $a_\pm$ in this section

$$V = \sqrt{\frac{Z_0}{2}}\,(a_+ + a_-) \tag{E2}$$

$$I = \frac{1}{\sqrt{2Z_0}}\,(a_- - a_+)\,. \tag{E3}$$

Here Z_0 is impedance of the transmission line. Like a_m, the squares of the amplitudes a_+^2 and a_-^2 are the outward and inward-going, time-averaged power in the transmission line. This is easily checked by computing the power into the microwave port

$$V^*I + VI^* = |a_-|^2 - |a_+|^2\,. \tag{E4}$$

Substituting Equations E2 and E3 into Equation E1 and collecting terms we find the S-matrix

$$\begin{pmatrix} a_+ \\ \mathbf{a}_+ \end{pmatrix} = \underbrace{\begin{pmatrix} \frac{Y_0 - Y}{Y_0 + Y} & -\frac{\sqrt{2Y_0}}{Y_0+Y}\mathbf{x}_1^\top \\ \frac{\sqrt{2Y_0}}{Y_0+Y}\mathbf{x}_2 & \text{X} + \frac{1}{Y_0+Y}\mathbf{x}_2\mathbf{x}_1^\top \end{pmatrix}}_{S} \begin{pmatrix} a_- \\ \mathbf{a}_- \end{pmatrix} \tag{E5}$$

where $Y_0 = Z_0^{-1}$. From reciprocity $S = S^\top$ we find $\mathbf{x} \equiv \mathbf{x}_2 = -\mathbf{x}_1$ and therefore

$$S = \begin{pmatrix} r_{\mu\mu} & t_{1\mu} & t_{2\mu} & \cdots \\ t_{1\mu} & r_{11} & t_{21} & \\ t_{2\mu} & t_{21} & r_{22} & \\ \vdots & & & \ddots \end{pmatrix} = \begin{pmatrix} \frac{Y_0 - Y}{Y_0 + Y} & \frac{\sqrt{2Y_0}}{Y_0+Y}\mathbf{x}^\top \\ \frac{\sqrt{2Y_0}}{Y_0+Y}\mathbf{x} & \text{X} + \frac{1}{Y_0+Y}\mathbf{x}\mathbf{x}^\top \end{pmatrix}. \tag{E6}$$

The first component of S connecting a_- and a_+ is the reflection S-parameter S_{11} in the absence of reflections in the network (such as off a second transducer). The component of S connecting a_- to the SH0 coefficient a_{b} is $t_{\text{b}\mu}$. Its magnitude is conveniently expressed

$$|t_{\text{b}\mu}| = \sqrt{1 - |S_{11}|^2}\,\frac{|x_{\text{b}}|}{\sqrt{2G}} \tag{E7}$$

where x_{b} is the SH0 component of $\mathbf{x}$ and is the coefficient a_{b} for a 1 V drive. $2G\,|V|^2$ is the total power dissipated by the transducer.

Appendix F: De-embedding $t_{b\mu}$, α, and r_{bb} from S_{21}

When making a transducer, especially one embedded in a network, *e.g.*, a transducer coupled to a resonator, it is tempting to be satisfied with a well-matched S_{11}. Suppression of $|S_{11}|$, *i.e.*, low microwave reflections, seems to imply that microwaves are being converted to mechanical waves and that the device is efficient. Under this prescription, one would choose an IDT's width and simply tune its length until it is matched. This procedure does not produce efficient devices.

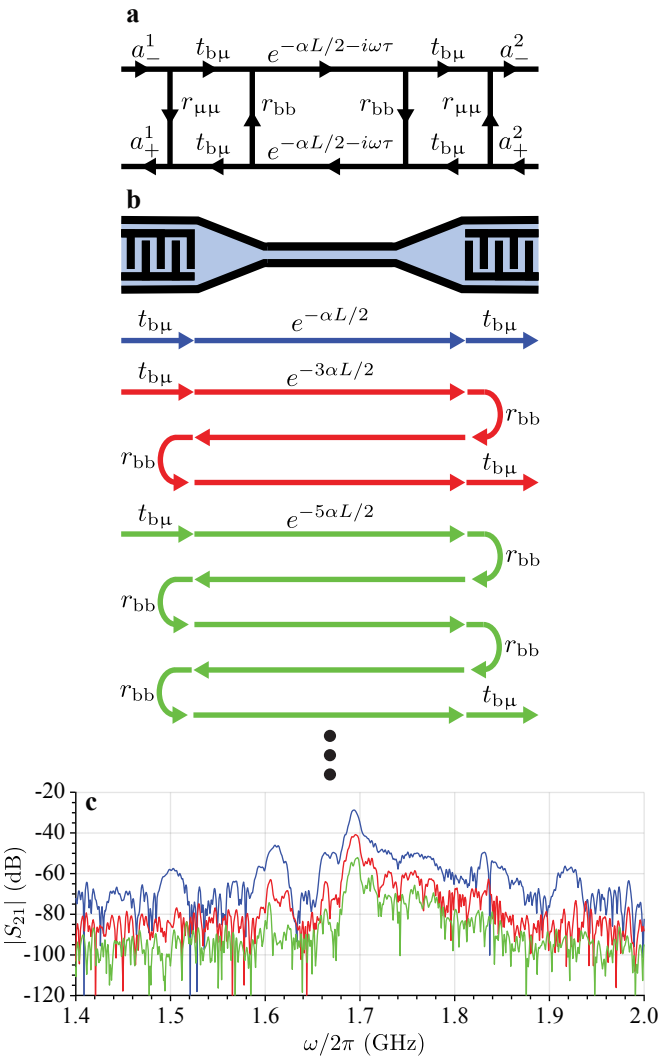

FIG. 8. **a.** Signal-flow graph for a two-port device. **b.** Paths for the single, triple, and quintuple-transit (colored blue, red, and green respectively) corresponding to the S_{21} curves of matching color in **c.** **c.** S_{21} filtered by path.

A strong S_{11} dip is a *necessary* but insufficient condition for efficiency ($|t_{b\mu}|^2 \to 1$). In a microwave or phononic network, reflections can strongly modify the response of a component. Resonance can enhance the transmission through the device. If network performance is the prime and only concern, measuring a resonator's intracavity phonon number against microwave input power, for example, will suffice. But if the goal is to make a transducer which can serve as a general component, one that can be embedded in an arbitrary network and the response accurately predicted, we need to de-embed the transducer's response from the larger network response.

In Appendix E, we describe how the full scattering matrix S can be computed by the FEM. In Section IV, we show that transmission into the SH0 mode exceeds the total transmission into all other modes by 10 dB. This allows us to reduce the S matrix of Equation E6 to two-ports

$$S = \begin{pmatrix} r_{\mu\mu} & t_{b\mu} \\ t_{b\mu} & r_{bb} \end{pmatrix}. \tag{F1}$$

The S-matrix for the waveguide is

$$S_{wg} = \begin{pmatrix} e^{-\alpha L/2-i\omega\tau} & 0 \\ 0 & e^{-\alpha L/2-i\omega\tau} \end{pmatrix} \tag{F2}$$

where $\tau = L/v_g$ is the transit time of the waveguide. The devices measured in Section V consist of a transducer, waveguide, and transducer. These components are cascaded in the signal flow graph in Figure 8a which can be reduced by standard methods [57] to find

$$S_{11} = r_{\mu\mu} + \frac{t_{b\mu}^2 r_{bb} e^{-\alpha L-2i\omega\tau}}{1 - r_{bb}^2 e^{-\alpha L-2i\omega\tau}} \tag{F3}$$

and

$$S_{21} = \frac{t_{b\mu}^2 e^{-\alpha L/2-i\omega\tau}}{1 - r_{bb}^2 e^{-\alpha L-2i\omega\tau}} \tag{F4}$$

where ports 1 and 2 are the electrical port of the first and second transducer. The second term in our expression for S_{11} comes from reflections r_{bb} and gives rise to the Fabry-Pérot peaks found on the blue side of ω_s in Figure 4c.

The impulse response $h(t)$ is computed by inverse Fourier transforming S_{21}. Expanding $\left(1 - r_{bb}^2 e^{-\alpha L-2i\omega\tau}\right)^{-1}$ to $\sum_n r_{bb}^{2n} e^{-n\alpha L-2in\omega\tau}$, each term represents an echo in the impulse response in Figure 4e. These echoes and the paths they take are diagrammed in Figure 8b.

Since the $L = 800$ μm device is long enough to resolve the echoes, the amplitudes of the echoes can be analyzed directly in the frequency domain by filtering out each echo in Figure 4e associated with a path in Figure 8b and taking the Fourier transform. The results of this procedure are inset to Figure 4e but are reproduced larger here for clarity. The transmission factor $t_{b\mu}^2 \exp(-\alpha L/2)$ is extracted from the first transit plotted in blue.

Appendix G: Insertion loss from impedance mismatch

In Section V we attribute a fraction of the insertion loss to impedance mismatch between the transducers and

transmission lines. This mismatch in Figure 4d is labeled the *two-port mismatch*. Derived below, this quantity is the average of the ratios of the power dissipated by each transducer over the incident microwave power $1 - |S_{11}|^2/2 - |S_{22}|^2/2$.

For any lossy, passive system

$$|S_{11}|^2 + |S_{12}|^2 < 1 \tag{G1}$$

and

$$|S_{22}|^2 + |S_{21}|^2 < 1. \tag{G2}$$

Summing these conditions and assuming reciprocity, i.e. $S_{21} = S_{12}$ we have

$$|S_{11}|^2 + |S_{22}|^2 + 2|S_{21}|^2 < 2 \tag{G3}$$

Rearranging the above expression we get

$$|S_{21}|^2 < 1 - |S_{11}|^2/2 - |S_{22}|^2/2 \tag{G4}$$

The right-hand side which sets an upperbound on S_{21} is the two-port mismatch.

[1] D. A. Fuhrmann, S. M. Thon, H. Kim, D. Bouwmeester, P. M. Petroff, A. Wixforth, and H. J. Krenner, Dynamic modulation of photonic crystal nanocavities using gigahertz acoustic phonons, Nature Photonics **5**, 605 (2011).

[2] O. Couto Jr, S. Lazić, F. Iikawa, J. Stotz, U. Jahn, R. Hey, and P. Santos, Photon anti-bunching in acoustically pumped quantum dots, Nature Photonics **3**, 645 (2009).

[3] D. A. Golter, T. Oo, M. Amezcua, K. A. Stewart, and H. Wang, Optomechanical quantum control of a nitrogen-vacancy center in diamond, Physical Review Letters **116**, 143602 (2016).

[4] S. J. Whiteley, G. Wolfowicz, C. P. Anderson, A. Bourassa, H. Ma, M. Ye, G. Koolstra, K. J. Satzinger, M. V. Holt, F. J. Heremans, *et al.*, Spin–phonon interactions in silicon carbide addressed by gaussian acoustics, Nature Physics **15**, 490 (2019).

[5] M. Weiler, H. Huebl, F. S. Goerg, F. D. Czeschka, R. Gross, and S. T. B. Goennenwein, Spin pumping with coherent elastic waves, Physical Review Letters **108**, 176601 (2012).

[6] L. Fan, C.-L. Zou, N. Zhu, and H. X. Tang, Spectrotemporal shaping of itinerant photons via distributed nanomechanics, Nature Photonics **13**, 323 (2019).

[7] Q. Liu, H. Li, and M. Li, Electromechanical Brillouin scattering in integrated optomechanical waveguides, Optica **6**, 778 (2019).

[8] S. A. Tadesse and M. Li, Sub-optical wavelength acoustic wave modulation of integrated photonic resonators at microwave frequencies, Nature Communications **5**, 5402 (2014).

[9] D. B. Sohn, S. Kim, and G. Bahl, Time-reversal symmetry breaking with acoustic pumping of nanophotonic circuits, Nature Photonics **12**, 91 (2018).

[10] M. Merklein, B. Stiller, K. Vu, S. J. Madden, and B. J. Eggleton, A chip-integrated coherent photonic-phononic memory, Nature Communications **8**, 574 (2017).

[11] A. Vainsencher, K. J. Satzinger, G. A. Peairs, and A. N. Cleland, Bi-directional conversion between microwave and optical frequencies in a piezoelectric optomechanical device, Applied Physics Letters **109**, 033107 (2016).

[12] J. Bochmann, A. Vainsencher, D. D. Awschalom, and A. N. Cleland, Nanomechanical coupling between microwave and optical photons, Nature Physics **9**, 712 (2013).

[13] K. C. Balram, M. I. Davanço, B. R. Ilic, J.-H. Kyhm, J. D. Song, and K. Srinivasan, Acousto-Optic Modulation and Optoacoustic Gating in Piezo-Optomechanical Circuits, Physical Review Applied **7**, 024008 (2017).

[14] M. Forsch, R. Stockill, A. Wallucks, I. Marinković, C. Gärtner, R. A. Norte, F. van Otten, A. Fiore, K. Srinivasan, and S. Gröblacher, Microwave-to-optics conversion using a mechanical oscillator in its quantum ground state, Nature Physics **16**, 69 (2020).

[15] W. Jiang, R. N. Patel, F. M. Mayor, T. P. McKenna, P. Arrangoiz-Arriola, C. J. Sarabalis, J. D. Witmer, R. V. Laer, and A. H. Safavi-Naeini, Lithium niobate piezo-optomechanical crystals, Optica **6**, 845 (2019).

[16] C. J. Sarabalis, R. Van Laer, and A. H. Safavi-Naeini, Optomechanical antennas for on-chip beam-steering, Optics Express **26**, 22075 (2018).

[17] G. S. MacCabe, H. Ren, J. Luo, J. D. Cohen, H. Zhou, A. Sipahigil, M. Mirhosseini, and O. Painter, Phononic bandgap nano-acoustic cavity with ultralong phonon lifetime, arXiv preprint arXiv:1901.04129 (2019).

[18] M. Pechal, P. Arrangoiz-Arriola, and A. H. Safavi-Naeini, Superconducting circuit quantum computing with nanomechanical resonators as storage, Quantum Science and Technology **4**, 015006 (2018).

[19] C. T. Hann, C.-L. Zou, Y. Zhang, Y. Chu, R. J. Schoelkopf, S. M. Girvin, and L. Jiang, Hardware-efficient quantum random access memory with hybrid quantum acoustic systems, Physiscal Review Letters **123**, 250501 (2019).

[20] K. J. Satzinger, Y. P. Zhong, H.-S. Chang, G. A. Peairs, A. Bienfait, M.-H. Chou, A. Y. Cleland, C. R. Conner, É. Dumur, J. Grebel, I. Gutierrez, B. H. November, R. G. Povey, S. J. Whiteley, D. D. Awschalom, D. I. Schuster, and A. N. Cleland, Quantum control of surface acoustic-wave phonons, Nature **563**, 661 (2018).

[21] P. Arrangoiz-Arriola, E. A. Wollack, Z. Wang, M. Pechal, W. Jiang, T. P. McKenna, J. D. Witmer, R. Van Laer, and A. H. Safavi-Naeini, Resolving the energy levels of a nanomechanical oscillator, Nature **571**, 537 (2019).

[22] M. V. Gustafsson, T. Aref, A. F. Kockum, M. K. Ekstrom, G. Johansson, and P. Delsing, Propagating phonons coupled to an artificial atom, Science **346**, 207 (2014).

[23] K. Fang, M. H. Matheny, X. Luan, and O. Painter, Optical transduction and routing of microwave phonons in cavity-optomechanical circuits, Nature Photonics **10**, 489 (2016).

[24] R. N. Patel, Z. Wang, W. Jiang, C. J. Sarabalis, J. T. Hill, and A. H. Safavi-Naeini, Single-Mode Phononic

Wire, Physical Review Letters **121**, 040501 (2018).
[25] T. Manzaneque, R. Lu, Y. Yang, and S. Gong, Low-Loss and Wideband Acoustic Delay Lines, IEEE Transactions on Microwave Theory and Techniques **67**, 1379 (2019).
[26] E. Romero, R. Kalra, N. P. Mauranyapin, C. G. Baker, C. Meng, and W. P. Bowen, Propagation and Imaging of Mechanical Waves in a Highly Stressed Single-Mode Acoustic Waveguide, Physical Review Applied **11**, 064035 (2019).
[27] K. Lakin, G. Kline, and K. McCarron, High-Q microwave acoustic resonators and filters, IEEE Transactions on Microwave Theory and Techniques **41**, 2139 (1993).
[28] T. Manzaneque, R. Lu, Y. Yang, and S. Gong, An SH0 Lithium Niobate dispersive delay line for chirp compression-enabled low power radios, in *2017 IEEE 30th International Conference on Micro Electro Mechanical Systems (MEMS)* (IEEE, 2017) pp. 155–158.
[29] A. Y. Cleland, M. Pechal, P.-J. C. Stas, C. J. Sarabalis, E. A. Wollack, and A. H. Safavi-Naeini, Mechanical purcell filters for microwave quantum machines, Applied Physics Letters **115**, 263504 (2019).
[30] M. Eichenfield, J. Chan, R. M. Camacho, K. J. Vahala, and O. Painter, Optomechanical crystals, Nature **462**, 78 (2009).
[31] M. S. Kang, A. Brenn, and P. St.J. Russell, All-Optical Control of Gigahertz Acoustic Resonances by Forward Stimulated Interpolarization Scattering in a Photonic Crystal Fiber, Physical Review Letters **105**, 153901 (2010).
[32] C. G. Poulton, R. Pant, and B. J. Eggleton, Acoustic confinement and stimulated Brillouin scattering in integrated optical waveguides, Journal of the Optical Society of America B **30**, 2657 (2013).
[33] R. Van Laer, B. Kuyken, D. Van Thourhout, and R. Baets, Interaction between light and highly confined hypersound in a silicon photonic nanowire, Nature Photonics **9**, 199 (2015).
[34] E. A. Kittlaus, H. Shin, and P. T. Rakich, Large Brillouin amplification in silicon, Nature Photonics **10**, 463 (2016).
[35] P. Ovartchaiyapong, K. W. Lee, B. A. Myers, and A. C. B. Jayich, Dynamic strain-mediated coupling of a single diamond spin to a mechanical resonator, Nature communications **5**, 4429 (2014).
[36] R. H. Olsson III and I. El-Kady, Microfabricated phononic crystal devices and applications, Measurement Science and Technology **20**, 012002 (2009).
[37] S. Mohammadi and A. Adibi, On chip complex signal processing devices using coupled phononic crystal slab resonators and waveguides, AIP Advances **1**, 041903 (2011).
[38] W. Fu, Z. Shen, Y. Xu, C.-L. Zou, R. Cheng, X. Han, and H. X. Tang, Phononic integrated circuitry and spinorbit interaction of phonons, Nature Communications **10**, 2743 (2019).
[39] A. V. Korovin, Y. Pennec, M. Stocchi, D. Mencarelli, L. Pierantoni, T. Makkonen, J. Ahopelto, and B. D. Rouhani, Conversion between surface acoustic waves and guided modes of a quasi-periodic structured nanobeam, Journal of Physics D: Applied Physics **52**, 32LT01 (2019).
[40] A. Siddiqui, R. H. Olsson, and M. Eichenfield, Lamb Wave Focusing Transducer for Efficient Coupling to Wavelength-Scale Structures in Thin Piezoelectric Films, Journal of Microelectromechanical Systems **27**, 1054 (2018).
[41] W. Jiang, C. J. Sarabalis, Y. D. Dahmani, R. N. Patel, F. M. Mayor, T. P. McKenna, R. Van Laer, and A. H. Safavi-Naeini, Efficient bidirectional piezo-optomechanical transduction between microwave and optical frequency, arXiv preprint arXiv:1909.04627 (2019).
[42] R. S. Weis and T. K. Gaylord, Lithium niobate: Summary of physical properties and crystal structure, Applied Physics A Solids and Surfaces **37**, 191 (1985).
[43] A. S. Andrushchak, B. G. Mytsyk, H. P. Laba, O. V. Yurkevych, I. M. Solskii, A. V. Kityk, and B. Sahraoui, Complete sets of elastic constants and photoelastic coefficients of pure and MgO-doped lithium niobate crystals at room temperature, Journal of Applied Physics **106**, 073510 (2009).
[44] I. Kuznetsova, B. Zaitsev, S. Joshi, and I. Borodina, Investigation of acoustic waves in thin plates of lithium niobate and lithium tantalate, IEEE Transactions on Ultrasonics, Ferroelectrics and Frequency Control **48**, 322 (2001).
[45] C. J. Sarabalis, Y. D. Dahmani, A. Y. Cleland, and A. H. Safavi-Naeini, The role of resonance and bandgaps in high k^2_{eff} transducers, arXiv preprint arXiv:1904.04981 (2019).
[46] B. A. Auld, *Acoustic fields and waves in solids, Volume II*, 2nd ed. (Robert E. Krieger Publishing Company, Malabar, Florida, 1990).
[47] B. A. Auld, *Acoustic fields and waves in solids, Volume I*, 2nd ed. (Robert E. Krieger Publishing Company, Malabar, Florida, 1990).
[48] G. Vidal-Alvarez, A. Kochhar, and G. Piazza, Delay lines based on a suspended thin film of X-cut lithium niobate, in *2017 IEEE International Ultrasonics Symposium (IUS)* (IEEE, 2017) pp. 1–4.
[49] Y. Yang, R. Lu, T. Manzaneque, and S. Gong, 1.7 GHz Y-Cut Lithium Niobate MEMS Resonators with FoM of 336 and fQ of 9.15×10^{12}, in *2018 IEEE/MTT-S International Microwave Symposium - IMS* (IEEE, 2018) pp. 563–566.
[50] C. S. Hartmann, D. T. Bell, and R. C. Rosenfeld, Impulse model design of acoustic surface-wave filters, IEEE Transactions on Microwave Theory and Techniques **21**, 162 (1973).
[51] K.-y. Hashimoto, ed., *RF bulk acoustic wave filters for communications* (Artech House, 2009) Chap. 3, p. 57.
[52] R. Aigner *et al.*, Bringing baw technology into volume production: The ten commandments and the seven deadly sins, in *IEEE Int. Symp. Acoust. Wave. Dev. for Future Mobile Communication Syst* (2007).
[53] C.-M. Lin, T.-T. Yen, Y.-J. Lai, V. V. Felmetsger, M. A. Hopcroft, J. H. Kuypers, and A. P. Pisano, Temperature-compensated aluminum nitride lamb wave resonators, IEEE transactions on ultrasonics, ferroelectrics, and frequency control **57**, 524 (2010).
[54] J. D. Larson, P. D. Bradley, S. Wartenberg, and R. C. Ruby, Modified butterworth-van dyke circuit for fbar resonators and automated measurement system, in *2000 IEEE Ultrasonics Symposium. Proceedings. An International Symposium (Cat. No. 00CH37121)*, Vol. 1 (IEEE, 2000) pp. 863–868.
[55] F. V. Pop, A. S. Kochhar, G. Vidal-Alvarez, and G. Piazza, Laterally vibrating lithium niobate mems resonators with 30% electromechanical coupling coefficient, in *2017 IEEE 30th International Conference on Micro Electro Mechanical Systems (MEMS)* (IEEE, 2017) pp.

966–969.
[56] G. B. Arfken and H. J. Weber, *Mathematical methods for physicists* (AAPT, 1999).
[57] D. M. Pozar, *Microwave Engineering*, 4th ed. (John Wiley & Sons, Inc., Hoboken, New Jersey, 2012).